

Three-dimensional Pentagon Carbon with a genesis of emergent fermions

Chengyong Zhong,¹ Yuanping Chen,^{1*} Zhi-Ming Yu,² Yuee Xie,¹ Han Wang,³
Shengyuan A. Yang,^{2*} Shengbai Zhang³

¹ *School of Physics and Optoelectronics, Xiangtan University, Xiangtan, 411105, Hunan, China*

² *Research Laboratory for Quantum Materials, Singapore University of Technology and Design, Singapore 487372, Singapore*

³ *Department of Physics, Applied Physics, and Astronomy Rensselaer Polytechnic Institute, Troy, New York 12180, USA*

Carbon, the basic building block of our universe, enjoys a vast number of allotropic structures.

Owing to its bonding characteristic, most carbon allotropes possess the motif of hexagonal rings.

Here, with first-principles calculations, we discover a new metastable three-dimensional carbon

allotrope entirely composed of pentagon rings. The unique structure of this Pentagon Carbon

leads to extraordinary electronic properties, making it a cornucopia of emergent topological

fermions. Under lattice strain, Pentagon Carbon exhibits topological phase transitions, generating

a series of novel quasiparticles, from isospin-1 triplet fermions, to triply-degenerate fermions, and

further to concatenated Weyl-loop fermions. Its Landau level spectrum also exhibits distinct

features, including a huge number of almost degenerate chiral Landau bands, implying

pronounced magneto-transport signals. Our work not only discovers a remarkable carbon

allotrope with highly rare structural motifs, it also reveals a fascinating hierarchical particle

genesis with novel topological fermions beyond the Dirac and Weyl paradigm.

Corresponding authors: chenyp@xtu.edu.cn; shengyuan_yang@sutd.edu.sg;

Most stable carbon allotropes, including the prominent members such as graphite, diamond, carbon nanotube¹, and graphene², possess a motif of hexagonal rings due to the dominating sp^2 and sp^3 bonding character³. In contrast, the motif of pentagonal rings, although can appear in molecules such as fullerene⁴, is very rare in three-dimensional (3D) allotropes. This is partly due to the unfavorable bonding angles that may easily cause structural instability⁵, and also because the pentagonal motif does not readily fit into the 3D space group symmetry⁶. It seems unlikely to have a stable 3D carbon allotrope dominated by pentagonal carbon rings.

Meanwhile, the research on topological metals and semimetals (TMs) has been attracting tremendous interest⁷⁻¹⁴. In these materials, topologically protected quasiparticles emerge at protected band-crossing points around Fermi Level, giving rise to condensed matter realizations of many peculiar fermions with a variety of distinct electronic properties. For example, in Dirac and Weyl semimetals, the quasiparticles near the protected linear band-crossing points are direct analogues of the Dirac and Weyl fermions in relativistic quantum field theory, providing unique opportunities to study interesting high-energy physics phenomena such as chiral anomaly and gravitational anomaly in a table-top experiment¹⁵⁻¹⁸. The emergent topological fermions can be classified by the degeneracy of the band-crossing point, which dictates the number of internal degrees of freedom of the fermion. Dirac and Weyl fermions are associated with crossing points with four- and two-fold degeneracies¹⁹.²⁰. Importantly, the breaking of Lorentz symmetry at lattice scale makes it possible to have TMs that

can host new types of fermions with different degeneracies beyond the Dirac and Weyl fermions²¹⁻²³.

These new fermions are now actively searched for, and if realized, they are believed to host a wealth of exotic physical properties unprecedented in high-energy physics.

The search for TMs has been focused on compounds involving heavy elements^{7, 24, 25}, hoping that the strong spin-orbit coupling could help to achieve a nontrivial band structure. On the other hand, light elements such as carbon may offer a distinct alternative. For example, graphene is well-known with two-dimensional (2D) Dirac fermions²⁶. With negligible spin-orbit coupling, the real spin in carbon materials can be considered as a dumb degree of freedom²⁷. Then the fundamental time reversal operation (\mathcal{T}) here satisfies $\mathcal{T}^2 = 1$, contrasting with $\mathcal{T}^2 = -1$ for the spinful case. Thus in terms of topological classifications, the nontrivial phases in carbon would be fundamentally distinct from those in spin-orbit-coupled systems. Indeed, previous studies have identified a few TM carbon allotropes with Weyl points^{28, 29}, nodal loops^{27, 29-32}, and even Weyl surfaces²⁸. Motivated by these observations, one may naturally wonder: Is it possible to also realize new types of topological fermions in carbon allotropes?

In this work, based on first-principles calculations, we propose a new 3D carbon allotrope, named as 3D Pentagon Carbon (3D-C5), which is entirely composed of pentagonal carbon rings. With nicely interlaced structures, the structure shows good stability, comparable to other metastable carbon allotropes. We characterize its phononic, mechanical, and electronic properties. At the

equilibrium state, Pentagon Carbon is a narrow-gap semiconductor. A semiconductor-metal quantum phase transition can be driven by an applied strain. Remarkably, at the critical transition point, three bands cross at a single Fermi point in the energy-momentum space, making the emergent low-energy fermions a novel type of isospin-1 triplet fermions. Beyond the transition, the single Fermi point splits into two triply-degenerate band-crossing points along the four-fold screw-rotational axis. The material is turned into a novel TM possessing another type of triply-degenerate fermions. When further breaking the screw-rotational symmetry, the triply-degenerate fermion points will transform into two inter-connected Hopf-link Weyl loops protected by the remaining mirror symmetry. We show that, for each case, the Landau level (LL) spectrum exhibits distinct features tied to the topological fermions, suggesting pronounced anomalies in magneto-transport experiment. In addition, we discuss a possible reaction pathway for the experimental synthesis of Pentagon Carbon.

Results

Lattice structure and stability. The structure of 3D Pentagon Carbon is shown in Fig. 1a , which can be viewed as formed by interlinking two orthogonal arrays of pentagon-ring nanoribbons and stacking them along the z -direction (Fig. 1b). After linking, the two nanoribbons share one (green-colored) atom. Hence in the Pentagon Carbon lattice, there are two kinds of carbon atoms, i.e. the sp^2 -hybridized (red- and blue-colored) atoms forming the backbones of the pentagon-ring

nanoribbons, and the sp^3 -hybridized (green-colored) atoms forming the linkage between ribbons.

The structure has the nonsymmorphic D_{4h}^{19} space group symmetry (No. 141, $I4_1/AMD$). Here an important symmetry element is the screw rotation \bar{C}_{4z} , which is a four-fold rotation along z followed by a fractional lattice-translation of $c\hat{z}/4$, where c is the lattice parameter in z -direction. The detailed structural properties are presented in Table 1, and are compared with several other (meta-) stable 3D carbon allotropes. One observes that the cohesive energy of Pentagon Carbon, although slightly higher than graphite and diamond, is less than $T6^{33}$ and $Bcc-C8^{34}$ and is comparable with Carbon Kagome Lattice^{35,36} structure. Due to its porous structure, the mass density of Pentagon Carbon is low ($\sim 2.18 \text{ g cm}^{-3}$), comparable with that of graphite. This is also correlated with its relatively low bulk modulus $\sim 257 \text{ GPa}$ compared with other allotropes (except for graphite), suggesting that external strain can be more easily applied. The phonon spectrum of Pentagon Carbon is also investigated, which shows no soft mode, confirming its dynamical stability (more analysis of lattice structure and stability can be found in Supplementary Fig. 1 and Note 1).

Electronic structure and quantum phase transition. Remarkably, Pentagon Carbon is also a material hosting a series of novel topological fermions beyond the usual Dirac and Weyl fermions. The band structure in Fig. 2a shows that, in equilibrium state, it is a narrow-gap semiconductor with a small energy gap $\sim 21.4 \text{ meV}$. The electronic structure shows strong anisotropy between in-plane

(xy) and out-of-plane (z) directions, in accordance with the crystal structural anisotropy. Focusing on the Γ point, there are two valence bands (heavy-hole and light-hole) and a single conduction band at low energy, with the conduction band and the light-hole valence band almost crossing linearly. Note that the degeneracy of the two valence bands at Γ is dictated by symmetry: the two states belong to a two-dimensional irreducible representation E_g of the D_{4h} group at Γ . In comparison, the conduction band belongs to the one-dimensional A_{1u} representation. Another salient feature is that the two valence bands are degenerate along the Γ -Z path (k_z -axis). This is because that there is remaining C_{4v} little group symmetry along this screw axis, such that the two-dimensional representation does not split according to the compatibility relation. From the analysis of wave-function and projected density of states (PDOS), we find that the low-energy states are mainly from the π orbitals of the sp^2 atoms (see Fig. 2f and Supplementary Fig. 2).

Since the semiconducting gap is small, a slight perturbation may close the gap and drive a semiconductor-to-metal phase transition (a tight-binding model analysis is given in Supplementary Fig. 3-4 and Note 2). In Figs. 2b-2d, we show band structures for three applied uniaxial strains $\varepsilon = 1\%$, -0.1% and -1% along the z -direction. One observes that indeed a semiconductor-metal phase transition is induced. A tensile strain drives the system to a semiconductor with wider gap, whereas a compressive strain drives the system towards a metal. Of particular interest is the change of band ordering at the Γ point. The A_{1u} singlet state and the E_g doublet switch their positions in energy

across the transition. Due to their different symmetry character, A_{1u} and E_g states cannot hybridize in the transition. Hence at the critical strain, we must have the three bands crossing at a single point, where the conduction and the light-hole bands have linear dispersion in the k_x - k_y plane; and all three bands have quadratic dispersion along the screw-axis. The 3D band structures in the Fig. 2i-2j clearly show the anisotropic feature around the triplet point.

Passing the critical point, the band ordering is inverted at Γ . However, the corresponding states at Z on the Brillouin zone boundary still have the original ordering. This band topology means that the two bands must cross each other between Γ and Z. Further, because the two bands still belong to different representations along the screw-axis, they must cross in a linear manner, with two triply-degenerate band-crossing points (one on each side of Γ), as confirmed in Fig. 2d. Therefore, the metallic phase represents a novel TM phase with a pair of triply-degenerate band-crossing points near the Fermi level. In such sense, the quantum phase transition may also be regarded as a topological phase transition from a trivial semiconductor phase to a TM phase.

We can define a Z_2 invariant to characterize this TM phase and the phase transition. Let Δ and Δ_Z be the values of the energy difference between A band and E band at Γ point and at Z point, respectively. Then a Z_2 invariant can be defined as $\chi = \text{sgn}(\Delta \cdot \Delta_Z) \in \{+1, -1\}$. $\chi = +1$ corresponds to the trivial case where a band crossing point does not need to occur, while $\chi = -1$ is the topologically nontrivial case where a triply-degenerate crossing point must exist between Γ and

Z. The topological phase transition from a trivial semiconductor phase to TM phase (as shown in Fig. 2) is thus characterized by χ changing from +1 to -1. The topological character is manifest in the sense that as long as the Z_2 invariant χ is well defined (i.e. symmetry is preserved) and does not change, the existence of the triply-degenerate crossing point and the linear band dispersion along k_z near the point are guaranteed and insensitive to system parameters and perturbations.

Emergent fermions and $\mathbf{k} \cdot \mathbf{p}$ model. Nontrivial band-crossing points are fascinating objects because the fermionic quasiparticles around these points necessarily have a multi-component structure, distinct from the usual Schrodinger fermions. The essential physics of these emergent fermions are characterized by the low-energy effective $\mathbf{k} \cdot \mathbf{p}$ model expanded around the crossing point.

Around the Γ point, we can construct the $\mathbf{k} \cdot \mathbf{p}$ model based on the three basis states of A_{1u} and E_g . Constrained by the D_{4h} symmetry group and the time reversal symmetry for a spinless system (as spin-orbit coupling is negligible for carbon), one obtains the $\mathbf{k} \cdot \mathbf{p}$ model up to k -quadratic order as

$$H(\mathbf{k}) = (C + D_1 k_z^2 + D_2 k_\perp^2) + \begin{bmatrix} \Delta + B_1 k_z^2 + B_2 k_\perp^2 & -iAk_x & -iAk_y \\ iAk_x & 0 & B_3 k_x k_y \\ iAk_y & B_3 k_x k_y & 0 \end{bmatrix}, \quad (1)$$

where the coefficients A , B_1 , B_2 , C , D_1 , D_2 , and Δ can be determined by fitting the DFT result. At transition point, $\Delta = 0$, the three bands cross at a single point, as illustrated in Fig. 3a. Then we can further simplify the model by keeping only the k -linear terms:

$$\mathcal{H}(\mathbf{k}) = A\mathbf{k} \cdot \boldsymbol{\lambda}, \quad (2)$$

where $\mathbf{k} = (k_x, k_y, 0)$, and

$$\lambda_x = \begin{bmatrix} 0 & -i & 0 \\ i & 0 & 0 \\ 0 & 0 & 0 \end{bmatrix}, \quad \lambda_y = \begin{bmatrix} 0 & 0 & -i \\ 0 & 0 & 0 \\ i & 0 & 0 \end{bmatrix}, \quad \lambda_z = \begin{bmatrix} 0 & 0 & 0 \\ 0 & 0 & -i \\ 0 & i & 0 \end{bmatrix}$$

are three of the eight Gell-Mann matrices corresponding to spin-1³⁷. This describes an isospin-1 triplet fermion moving in the xy -plane. The fermion is helical, with a well-defined helicity of ± 1 and 0 corresponding to the eigenvalues of the helicity operator $\mathbf{k} \cdot \boldsymbol{\lambda}/k$. The two branches with helicity ± 1 are massless while the remain one with helicity 0 has a flat dispersion, and these are constrained by the presence of an emergent “chiral symmetry” operation $\mathcal{C} = \text{diag}(1, -1, -1)$ with $\{\mathcal{H}(\mathbf{k}), \mathcal{C}\} = 0$. The finite mass term for $\Delta \neq 0$ breaks this symmetry, generating a mass for both ± 1 branches and gapping the spectrum.

Passing the critical point, the isospin-1 triplet fermion point split into two triply-degenerate points located at $k_z = \tau K_c$, as shown in Fig. 3b, where $\tau = \pm$ is an index labeling the two crossing points and $K_c = \sqrt{-\Delta/B_1}$ (note that we must have $\Delta < 0$ and $B_1 > 0$ to reproduce the band structure). The emergent triply-degenerate fermions around each crossing-point are described by the linearized model obtained from Eq. (1) as

$$H_\tau(\mathbf{q}) = \begin{bmatrix} 2\tau(B_1 + D_1)K_c q_z & -iAq_x & -iAq_y \\ iAq_x & 2\tau D_1 K_c q_z & 0 \\ iAq_y & 0 & 2\tau D_1 K_c q_z \end{bmatrix}, \quad (3)$$

where the wave vector \mathbf{q} is measured from the crossing point. One notes that in the direction perpendicular to the screw axis, i.e. in the q_x - q_y plane, the dispersion is the same as that for the

isospin-1 triplet fermion in Eq. (2). One finds that the triply-degenerate fermions basically inherit the structure of the triplet fermions but acquire one more degree of freedom, i.e. the motion along z -direction. In the meantime, they lose the well-defined helicity.

The two kinds of fermionic quasiparticles, the isospin-1 triplet fermions and the triply-degenerate fermions, are new types of emergent fermions. Unlike the Dirac and Weyl fermions studied before, these new fermions do not have direct analogues in the relativistic quantum field theory. The isospin-1 triplet fermion point is not topologically protected: it marks the critical point in the quantum phase transition. In contrast, the two triply-degenerate fermion points are protected by the nontrivial band topology and the four-fold screw axis. These features are schematically illustrated in Figs. 3a-3b.

When further breaking the screw-rotational symmetry, the double-degeneracy of the E band will be lifted; hence the triply-degenerate fermion point will disappear. However, note that the original A and E bands have different eigenvalues under the mirror operations M_{xz} and M_{yz} . Hence crossings between each split E band and A band in the mirror-invariant k_x - k_z and k_y - k_z planes will be protected if the respective mirror symmetry remains. For example, by an additional uniaxial strain along x -direction or along diagonal directions in the x - y plane, we find that, interestingly, the resulting band crossings form two orthogonal concatenated Weyl loops, which has the topology of a Hopf-link. As shown in Fig. 3c, for an additional tensile strain along the x -direction, one Weyl loop is

centered at the Γ point lying in the k_x - k_z plane, while the other loop is in the k_y - k_z plane and crosses the first Brillouin zone boundary. Around each point on the loop, the energy dispersion along two transverse directions is of the Weyl-like linear type, as shown in Fig. 3d. It needs to be emphasized that the band crossing forms the Weyl loop fermion, not Weyl fermion, because the inversion symmetry is still preserved. It is particularly interesting that the two Weyl loops form an inter-connected Hopf-link pattern. And these two loops are protected by the M_{xz} and M_{yz} mirror symmetries respectively. It should also be noted that there is no symmetry to pin these Weyl loops at a constant energy, and indeed, the energy varies along each loop.

Landau level spectrum. Topological character of the band structure can manifest when subjecting to a magnetic field³⁸⁻⁴⁰. For a 3D system, the electron motion in the plane perpendicular to the field is quantized into LLs. The dispersion along the field connects the levels to form dispersive Landau bands. For example, at each Weyl point, there is a gapless chiral Landau band, such that an additional parallel electric field will drive charge creation or depletion depending on the chirality. Since Weyl points appear in pairs of opposite chirality, the process leads to charge pumping between the Weyl points. This non-conservation of chiral charge at a single Weyl point is the well-known chiral anomaly^{14, 18, 40}. Experimentally, it manifests as a negative magnetoresistance, which has recently been demonstrated in Weyl semimetals^{15, 16}.

For Pentagon Carbon, considering a magnetic field along the screw axis such that the screw rotational symmetry is preserved. Focusing on the low-energy physics around the Γ point where the quantum phase transition occurs, we find that the LL spectrum exhibits drastic difference across the transition. As illustrated in Fig. 4a, one observes that in the semiconductor phase, the LL spectrum shows a spectral gap, typical for a semiconducting state. Remarkably, in the TM phase, there appear two chiral Landau bands crossing the spectral gap and crossing the location of the original triply-degenerate fermion points (see Fig. 4b). This is like that of a Weyl point, however, there is a marked difference: the chiral band here is in fact with a huge number of Landau bands nearly degenerate onto a single curve²¹. This behavior is due to the small values of the in-plane quadratic terms such as B_2 and B_3 . If one artificially increases these parameters, there will be a visible splitting between the almost degenerate Landau bands. Similar to chiral anomaly, a parallel \mathbf{E} -field would pump charges from one triply-degenerate point to the other. Due to the large number of the bands, it is expected to generate pronounced signals in magneto-transport experiment.

When further breaking the screw-rotational symmetry, the triply-degenerate fermion points disappear, giving rise to inter-connected Hopf-link Weyl loops. In the LL spectrum, we see that the main effect of the symmetry-breaking is to split the chiral Landau bands, as indicated in Fig. 4c. These interesting LL features reflect the evolution of the band-crossing points and will be useful for probing the quantum phase transition and the emergent topological fermions.

Discussion

Our work discovers a new metastable 3D carbon allotrope — the Pentagon Carbon, which exhibits a beautiful lattice structure entirely composed of pentagonal rings — a highly rare lattice motif for 3D crystals. Originating from this unique structure, there appear interesting quantum phase transitions and the associated novel emergent fermions. Remarkably, we reveal a fascinating transformation from isospin-1 triplet fermion point to triply-degenerate fermion point and finally to inter-connected Hopf-link Weyl loops.

Nontrivial band-crossing point is also predicted in a few recent works. Particularly, Bradlyn et al (Ref. 21) classified all possible degeneracy points at high-symmetry k-points for the 230 space groups in spin-orbit-coupled systems, and triple-degenerate points have also been found in a few materials with strong spin-orbit-coupling^{22, 41, 42}. The triply-degenerate points here are distinct from those previous examples in the following aspects: First, due to the negligible SOC, Pentagon Carbon is essentially a spinless system, and as we mentioned at the beginning, spinful and spinless systems belong to different symmetry/topological classes (For example, the time reversal operation has distinct properties between the two cases. And rotations for spinful systems will also operate on the spin degree of freedom, requiring a double group representation, distinct from spinless systems.); Second, while the degeneracy points in Ref. 21 are at high-symmetry points, here they are on symmetry lines (Γ -Z). Hence, without altering the symmetry, the latter is free to move along the

symmetry line by applying a strain with observable physical consequences, whereas the former is pinned at the high-symmetry k -points. A work by Heikkila and Volovik discussed possible triply-degenerate points in Bernal graphite²⁷, where each point connects four Dirac band-crossing lines with each line protected by a Z_2 invariant $N_1 = \pm 1$. In contrast, the triply-degenerate points in Pentagon Carbon are on a single band degeneracy line along k_z -axis (as in Fig. 3b); it is not a Dirac line because the dispersion is quadratic along the transverse directions, so the corresponding Z_2 invariant, as defined in Ref. 27, is trivial ($N_1 = 0$). The protection of the band degeneracy line and triply-degenerate point here has a qualitatively different physical origin, which is originated from the four-fold screw-rotational symmetry and band ordering topology, not present in Bernal graphite. We note that the different configurations of degeneracy lines in Bernal graphite and Pentagon Carbon precisely reflect their distinct symmetries: The arrangement of four Dirac lines with Z_2 indices $(-1, +1, +1, +1)$ observed in Bernal graphite is allowed by its three-fold rotational symmetry, but it is *not* compatible with the four-fold screw-rotation in Pentagon Carbon.

Here we focus on the effect of uniaxial strain in driving the phase transition. Other types of lattice deformation can also produce a similar effect, as long as the four-fold screw-rotational symmetry is preserved. For example, isotropic lattice strain or hydrostatic pressure can drive the phase transition with qualitatively similar features: the critical value is -1% for isotropic strain and 4.75 GPa for hydrostatic pressure. We also mention that like other carbon allotropes, Pentagon

Carbon has excellent mechanical property. From first-principles calculation, it shows a linear elastic regime up to $\pm 10\%$ strain (see Supplementary Fig. 5). Hence the strain-induced phase transitions discussed here should be readily achievable.

To guide experiment, we simulate X-ray diffraction (XRD) peaks of Pentagon Carbon and contrast them with those of representative carbon allotropes (see Supplementary Fig. 6). We also suggest a possible reaction route for the chemical synthesis. Molecules with pentagonal rings can be synthesized, e.g. in cyclopentadiene with different substitutes. Starting from 1,4-dibromocyclopentadiene, the cyclopentadiene building units can be linked into a 1D ribbon through Yamamoto polymerisation. The 1D ribbons could be functionalized with bromides and boronic acids which are connected into the 3D framework through Suzuki coupling (the details are described in Supplementary Fig. 7). Each step in this process is either already achieved or have a high chance to be achieved because of the existence of similar reactions. Given its energetic and dynamic stabilities and in view of the rapid progress in experimental techniques which have realized a number of carbon structures in recent decade^{34, 43}, we expect Pentagon Carbon could also be realized in the near future.

Methods

Computational methods: We performed first-principles calculations within the density functional theory (DFT) formalism as implemented in VASP code^{44, 45}. The potential of the core electrons and

the exchange-correlation interaction between the valence electrons are described, respectively, by the projector augmented wave⁴⁶ approach and the generalized gradient approximation (GGA) in the Perdew Burke-Ernzerhof (PBE)⁴⁷ implementation. The kinetic energy cutoff of 500 eV is employed. The atomic positions were optimized using the conjugate gradient method. The energy and force convergence criteria are set to be 10^{-5} eV and 10^{-2} eV Å⁻¹, respectively. The band structure and projected density of states (PDOS) were calculated using the primitive cell. The BZ was sampled with a $7 \times 7 \times 7$ Monkhorst-Pack (MP) special k -point grid for geometrical optimization. Phonon spectra are calculated using force-constants method, and the dynamical matrices are computed using the finite differences method in a $2 \times 2 \times 2$ supercell to eliminate errors in the low frequency modes (calculation with $3 \times 3 \times 3$ supercell is also carried out for verification). The force constants and phonon spectra were obtained using the Phonopy package⁴⁸. Calculation with the Heyd-Scuseria-Ernzerhof (HSE06)⁴⁹ hybrid functional is also performed to verify the band structure. The values of the band gap and the critical transition strain become larger compared with PBE results (the HSE06 gap is about 471 meV and the critical strain is about -2%), but the qualitative features of the bands and phase transitions remain the same (see Supplementary Fig. 8 and Note 3). The effect of van der Waals interaction is also tested and is found to be weak, e.g. by including the van der Waals interaction, the cohesive energy is decreased from -8.79 to -8.89 eV and the lattice constants are decreased by about 0.2% (see Supplementary Fig. 9).

Data availability: The data that support the findings of this study are available from the corresponding authors upon reasonable request.

Acknowledgements:

The authors thank the helpful discussions with Man-Fung Cheung, D. L. Deng, Shuai Yuan, Weiyu Xie, and Damien J. West. This work was supported by the National Natural Science Foundation of China (Nos. 51376005 and 11474243). SZ acknowledges the support by US DOE under Grant No. DE-SC0002623. ZMY and SAY are supported by the Singapore MOE Academic Research Fund Tier 1 (SUTD-T1-2015004) and Tier 2 (MOE2015-T2-2-144).

Author contributions:

Y.C. proposed the Pentagon Carbon. Y.C., S.A.Y. and S.Z. conceived the original ideas. C.Z., Y.C., Z.M.Y. and S.A.Y. conducted the calculations. Y.C. and S.Y. wrote the manuscript. All authors discussed the results and commented on the manuscript at all stages.

Additional information:

Competing financial interests: The authors declare no competing financial interests.

References:

1. Iijima S. Helical microtubules of graphitic carbon. *Nature* **354**, 56-58 (1991).
2. Geim A. K., Novoselov K. S. The rise of graphene. *Nat. Mater.* **6**, 183-191 (2007).
3. Hirsch A. The era of carbon allotropes. *Nat. Mater* **9**, 868-871 (2010).
4. Kroto H. W., Heath J. R., O'Brien S. C., Curl R. F., Smalley R. E. C60: Buckminsterfullerene. *Nature* **318**, 162-163 (1985).
5. Ewels C. P., Rocquefelte X., Kroto H. W., Rayson M. J., Briddon P. R., Heggie M. I. Predicting experimentally stable allotropes: Instability of penta-graphene. *Proc. Natl. Acad. Sci.* **112**, 15609-15612 (2015).
6. Dresselhaus M. S., Dresselhaus G., Jorio A. *Group theory: application to the physics of condensed matter*. Springer Science & Business Media (2007).
7. Wan X., Turner A. M., Vishwanath A., Savrasov S. Y. Topological semimetal and Fermi-arc surface states in the electronic structure of pyrochlore iridates. *Phys. Rev. B* **83**, 205101 (2011).
8. Soluyanov A. A., *et al.* Type-II Weyl semimetals. *Nature* **527**, 495-498 (2015).
9. Xu S. Y., *et al.* Discovery of a Weyl fermion semimetal and topological Fermi arcs. *Science* **349**, 613-617 (2015).
10. Turner A. M., Vishwanath A., Head C. O. Beyond band insulators: topology of semimetals and interacting phases. *Topological Insulators* **6**, 293-324 (2013).
11. Hasan M., Xu S., Neupane M. Topological insulators, topological crystalline insulators, topological Kondo insulators, and topological semimetals. *Topological Insulators: Fundamentals and Perspectives*, (2015).
12. Yang S. A., Pan H., Zhang F. Dirac and Weyl superconductors in three dimensions. *Phys. Rev. Lett.* **113**, 046401 (2014).

13. Yang S. A., Pan H., Zhang F. Chirality-Dependent Hall Effect in Weyl Semimetals. *Phys. Rev. Lett.* **115**, 156603 (2015).
14. Aji V. Adler-Bell-Jackiw anomaly in Weyl semimetals: Application to pyrochlore iridates. *Phys. Rev. B* **85**, 241101 (2012).
15. Huang X., *et al.* Observation of the Chiral-Anomaly-Induced Negative Magnetoresistance in 3D Weyl Semimetal TaAs. *Phys. Rev. X* **5**, 031023 (2015).
16. Parameswaran S. A., Grover T., Abanin D. A., Pesin D. A., Vishwanath A. Probing the Chiral Anomaly with Nonlocal Transport in Three-Dimensional Topological Semimetals. *Phys. Rev. X* **4**, 031035 (2014).
17. Nielsen H. B., Ninomiya M. The Adler-Bell-Jackiw anomaly and Weyl fermions in a crystal. *Phys. Lett. B* **130**, 389-396 (1983).
18. Son D. T., Spivak B. Z. Chiral anomaly and classical negative magnetoresistance of Weyl metals. *Phys. Rev. B* **88**, 104412 (2013).
19. Yang S. A. Dirac and Weyl Materials: Fundamental Aspects and Some Spintronics Applications. *SPIN* **06**, 1640003 (2016).
20. Young S. M., Zaheer S., Teo J. C. Y., Kane C. L., Mele E. J., Rappe A. M. Dirac Semimetal in Three Dimensions. *Phys. Rev. Lett.* **108**, (2012).
21. Bradlyn B., *et al.* Beyond Dirac and Weyl fermions: Unconventional quasiparticles in conventional crystals. *Science* **353**, aaf5037 (2016).
22. Chang G., *et al.* New fermions on the line in topological symmorphic metals. *Preprint at* <https://arxiv.org/abs/1605.06831>, (2016).
23. Orlita M., *et al.* Observation of three-dimensional massless Kane fermions in a zinc-blende crystal. *Nat. Phys.* **10**, 233-238 (2014).
24. Dai X. Weyl semimetals: A group family picture. *Nat. Mater.* **15**, 5-6 (2015).

25. Liu Z. K., *et al.* Evolution of the Fermi surface of Weyl semimetals in the transition metal pnictide family. *Nat. Mater.* **15**, 27-31 (2016).
26. Novoselov K. S., *et al.* Two-dimensional gas of massless Dirac fermions in graphene. *Nature* **438**, 197-200 (2005).
27. Heikkilä T. T., Volovik G. E. Nexus and Dirac lines in topological materials. *New J. Phys* **17**, 093019 (2015).
28. Zhong C., Chen Y., Xie Y., Yang S. A., Cohen M. L., Zhang S. B. Towards three-dimensional Weyl-surface semimetals in graphene networks. *Nanoscale* **8**, 7232-7239 (2016).
29. Chen Y., *et al.* Nanostructured Carbon Allotropes with Weyl-like Loops and Points. *Nano Lett.* **15**, 6974-6978 (2015).
30. Weng H., *et al.* Topological node-line semimetal in three-dimensional graphene networks. *Phys. Rev. B* **92**, 045108 (2015).
31. Wang J. T., Weng H., Nie S., Fang Z., Kawazoe Y., Chen C. Body-Centered Orthorhombic C₁₆: A Novel Topological Node-Line Semimetal. *Phys. Rev. Lett.* **116**, 195501 (2016).
32. Cheng Y., *et al.* Body-Centered Tetragonal C₁₆ : A Novel Topological Node-Line Semimetallic Carbon Composed of Tetrarings. *Small* **13**, 1602894-n/a (2017).
33. Zhang S., Wang Q., Chen X., Jena P. Stable three-dimensional metallic carbon with interlocking hexagons. *Proc. Natl. Acad. Sci.* **110**, 18809-18813 (2013).
34. Johnston R. L., Hoffmann R. Superdense carbon, C₈: supercubane or analog of γ -silicon? *J. Am. Chem. Soc.* **111**, 810-819 (1989).
35. Chen Y., *et al.* Carbon kagome lattice and orbital-frustration-induced

- metal-insulator transition for optoelectronics. *Phys. Rev. Lett.* **113**, 085501 (2014).
36. Zhong C., Xie Y., Chen Y., Zhang S. Coexistence of flat bands and Dirac bands in a carbon-Kagome-lattice family. *Carbon* **99**, 65-70 (2016).
 37. Georgi H., Jagannathan K. Lie Algebras in Particle Physics. *Am. J. Phys.* **50**, 1053-1053 (1982).
 38. Jeon S., *et al.* Landau quantization and quasiparticle interference in the three-dimensional Dirac semimetal Cd₃As₂. *Nat. Mater.* **13**, 851-856 (2014).
 39. Hosur P., Qi X. Recent developments in transport phenomena in Weyl semimetals. *C. R. Phys.* **14**, 857-870 (2013).
 40. Yu Z. M., Yao Y., Yang S. A. Predicted Unusual Magnetoresponse in Type-II Weyl Semimetals. *Phys. Rev. Lett.* **117**, 077202 (2016).
 41. Zhu Z., Winkler G. W., Wu Q., Li J., Soluyanov A. A. Triple Point Topological Metals. *Phys. Rev. X* **6**, 031003 (2016).
 42. Weng H., Fang C., Fang Z., Dai X. Topological semimetals with triply degenerate nodal points in θ -phase tantalum nitride. *Phys. Rev. B* **93**, 241202 (2016).
 43. Liu P., Cui H., Yang G. W. Synthesis of Body-Centered Cubic Carbon Nanocrystals. *Crystal Growth & Design* **8**, 581-586 (2008).
 44. Kresse G., Furthmüller J. Efficiency of ab-initio total energy calculations for metals and semiconductors using a plane-wave basis set. *Comp. Mater. Sci.* **6**, 15-50 (1996).
 45. Kresse G., Hafner J. Ab initio molecular dynamics for liquid metals. *Phys. Rev. B* **47**, 558-561 (1993).
 46. Blöchl P. E. Projector augmented-wave method. *Phys. Rev. B* **50**, 17953-17979 (1994).

47. Perdew J. P., *et al.* Atoms, molecules, solids, and surfaces: Applications of the generalized gradient approximation for exchange and correlation. *Phys. Rev. B* **46**, 6671-6687 (1992).
48. Togo A., Oba F., Tanaka I. First-principles calculations of the ferroelastic transition between rutile-type and CaCl₂-type SiO₂ at high pressures. *Phys. Rev. B* **78**, 134106 (2008).
49. Heyd J., Scuseria G. E., Ernzerhof M. Hybrid functionals based on a screened Coulomb potential. *The Journal of Chemical Physics* **118**, 8207-8215 (2003).

Figures and Tables

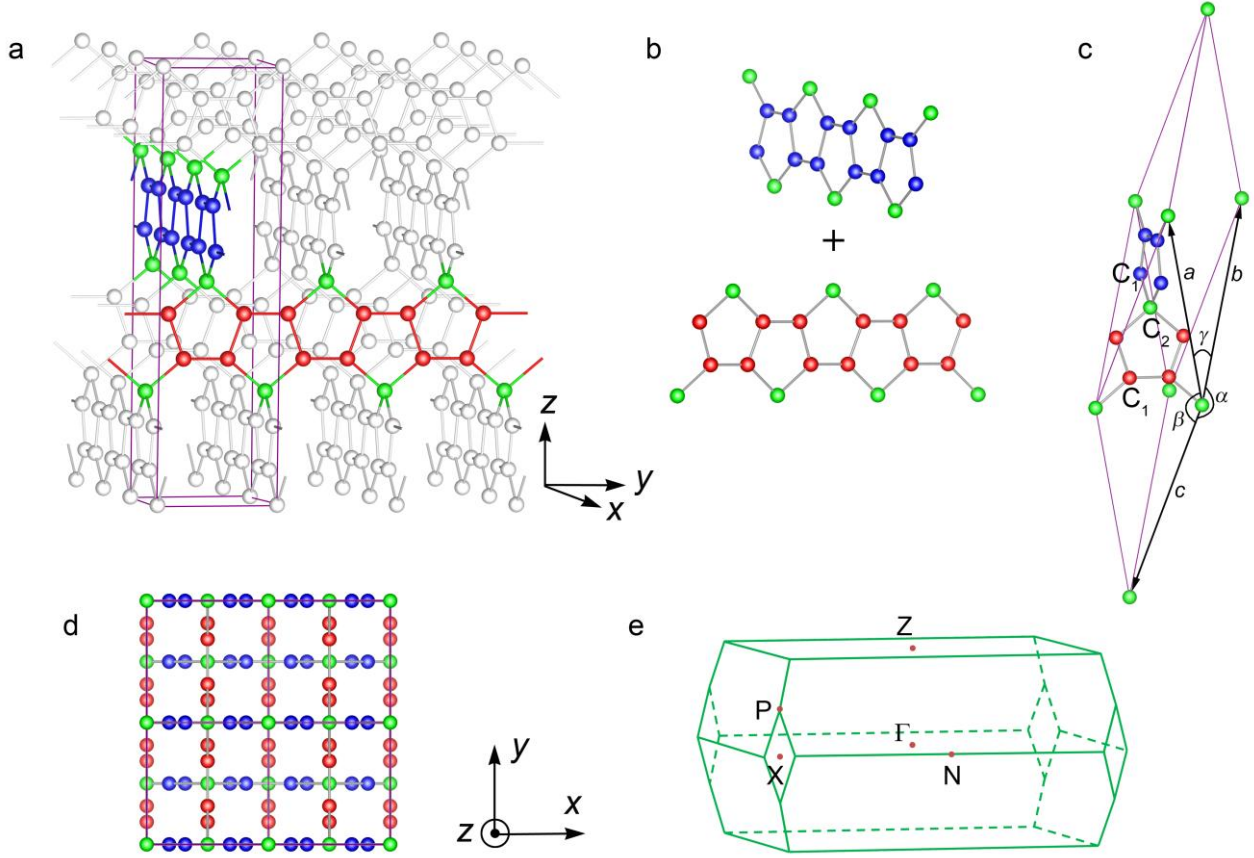


Figure 1. Crystal structure and Brillouin Zone of 3D Pentagon Carbon. (a) Structure of 3D Pentagon Carbon, where the purple lines depict the conventional unit cell, and the red and blue Carbon atoms form mutually orthogonal armchair chains which are linked by the green atoms. This structure can also be viewed as composed of orthogonal pentagonal-rings sharing the vertex green atoms, as shown in (b). (c) Primitive cell of 3D Pentagon Carbon. The red and blue atoms are marked as C1 sites and the green atoms are marked as C2 sites, indicating their different orbital hybridization character. The lattice parameters of the primitive cell are $a = b = c = 7.15 \text{ \AA}$, $\alpha = \beta = 149.86^\circ$, $\gamma = 43.11^\circ$. (d) Top view (from z -axis) of the structure, showing that the red and blue armchair chains are mutually orthogonal. (e) Brillouin Zone of the primitive cell along with the high-symmetry points marked.

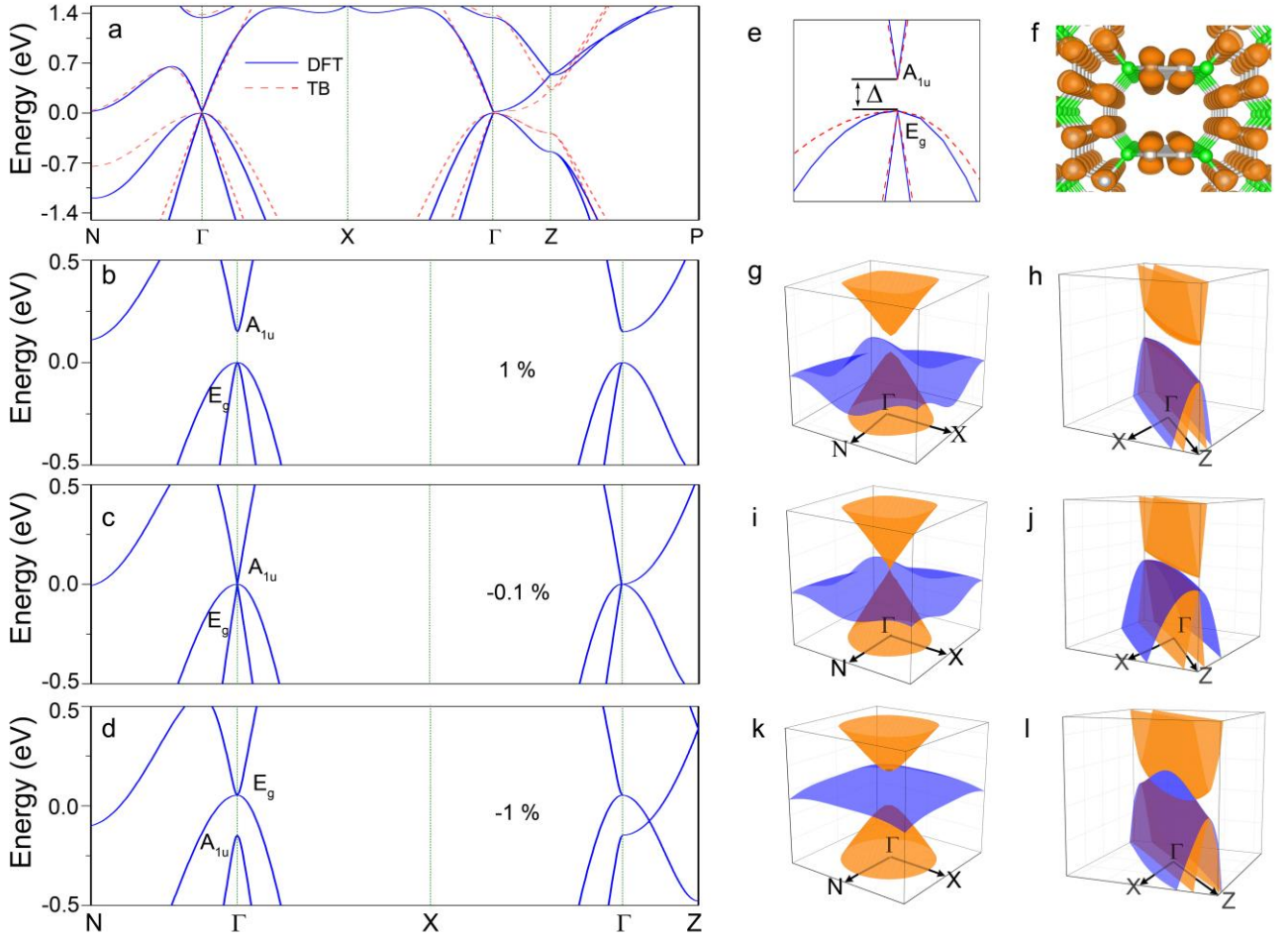


Figure 2| Electronic band structure of 3D Pentagon Carbon. (a) Band structure of 3D Pentagon Carbon, as from DFT calculation (blue solid line) and from tight-binding model (red dashed line). (b-d) The band structures of 3D Pentagon Carbon under uniaxial strain along z -direction with $\varepsilon = 1\%$, -0.1% and -1% , respectively. (e) The zoom-in view of band structure around the Γ point in (a) along N - Γ - X . The two degenerate valence bands at Γ belong to the two-dimensional irreducible representation E_g , and the lowest conduction band belongs to the one-dimensional A_{1u} representation. (f) The charge density distribution for states near the Fermi level in (a), indicating these states are mainly from π orbitals of the sp^2 hybridized atoms. (g/i/k-h/j/l) The 3D band structures on the N - Γ - X and the X - Γ - Z planes corresponding to (b/c/d), respectively.

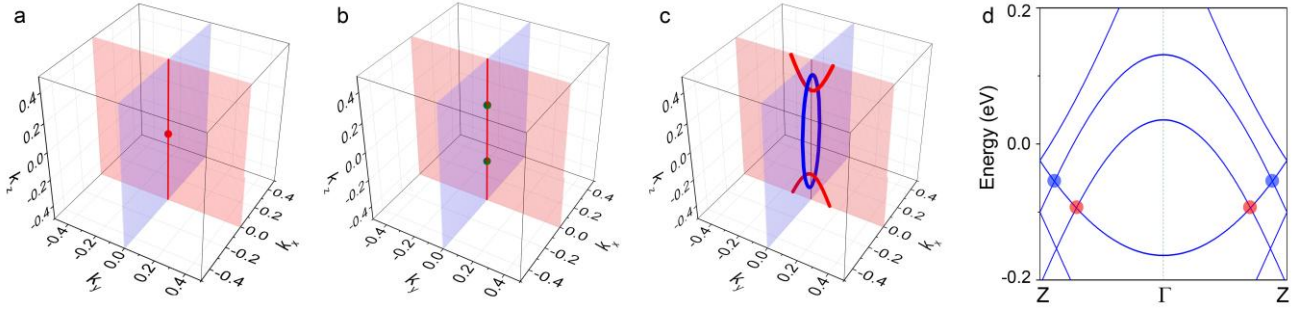


Figure 3. Emergent fermions in Pentagon Carbon. Schematic of the band-crossing evolution in reciprocal space, from (a) a single isospin-1 triplet fermion point at the Brillouin zone center, to (b) two triply-degenerate fermion points along k_z -axis (one on each side of Γ point), further to (c) two inter-connected (Hopf-link) Weyl loops (with one Weyl loop being centered at Γ point, while the other loop crossing the first Brillouin zone boundary). In (a) and (b), the red line along the k_z -axis marks the (two-fold) band degeneracy line protected by the four-fold screw-rotational symmetry. Note that the dispersion transverse to this line (i.e. in k_x - k_y plane) is of quadratic type (which can be observed from Fig. 2). (d) The DFT band structure of 3D Pentagon Carbon under broken four-fold screw-rotational symmetry (with uniaxial strain of -1% along z -axis followed by 1% tensile strain along x -axis). The red (blue) dot indicates the crossing point of red (blue) circle in (c) with the k_z -axis.

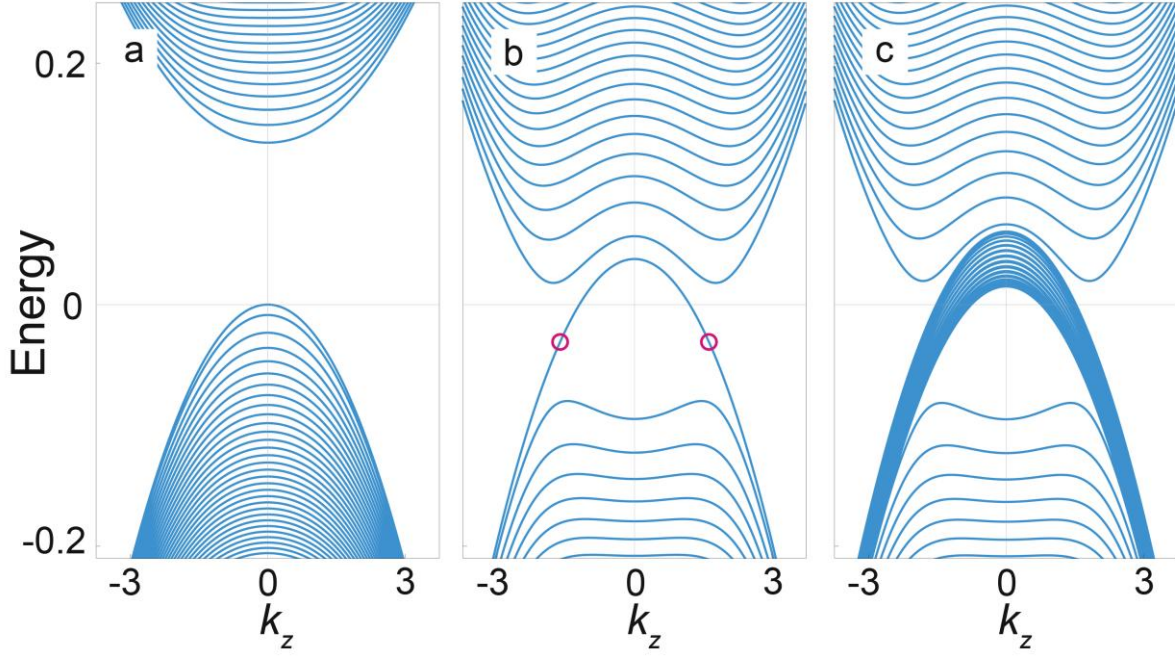
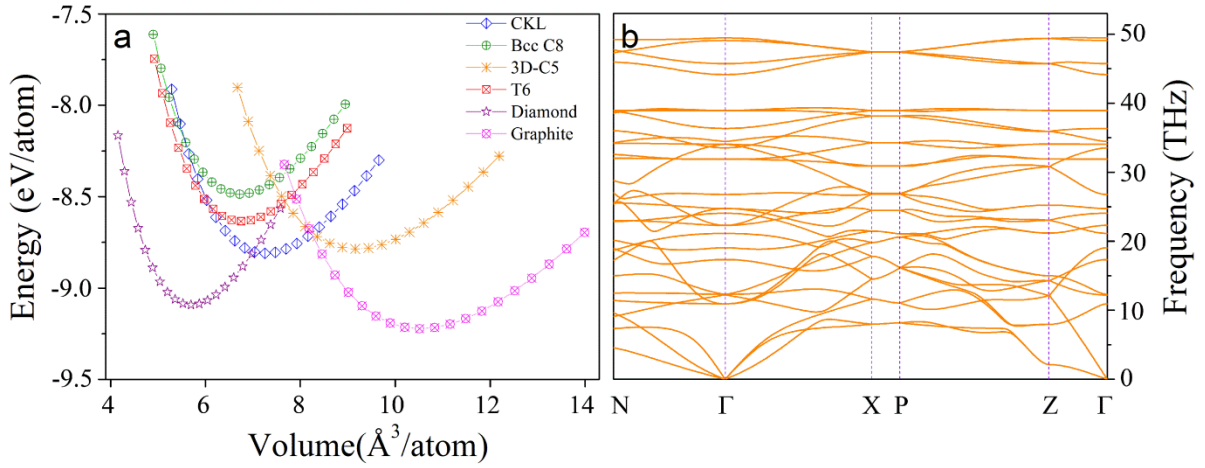


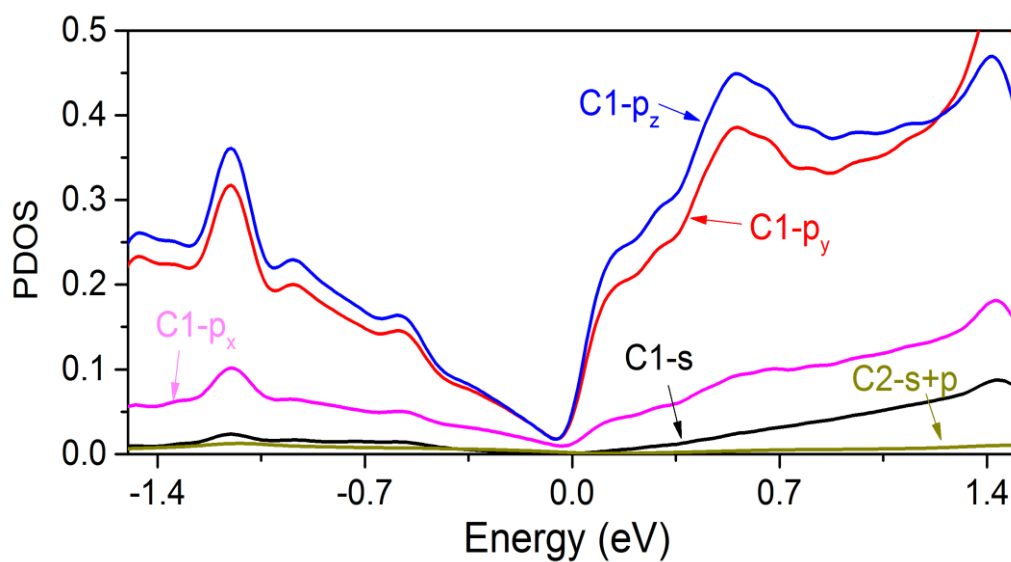
Figure 4. Landau level spectra. Landau level spectra for (a) the semiconductor phase, (b) the TM phase (corresponding to Fig. 2d), and (c) the TM phase with further screw-rotational symmetry breaking (corresponding to Fig. 3c). The magnetic field is along the z -direction. The red circles in (b) indicate the location of the two triply-degenerate fermion points (see Fig. 3b).

System	Space Group	$d (sp^2)$	$d (sp^3)$	$\theta (sp^2)$	$\theta (sp^3)$	ρ	B	E_{coh}
CKL	$F6_3/MMC$		1.53,1.50		60.0,115.1,117.7	2.75	327	-8.81
Bcc C8	$P4/MMM$		1.52,1.58,1.59		90.0,117.6,139.1	2.97	343	-8.49
3D-C5	$I4_1/AMD$	1.37,1.44	1.53	109.7,110.3,140.1	100.1,114.3	2.18	257	-8.79
T6	$P4_2/MMC$	1.34	1.54	115.1,122.5	106.7,115.1	2.95	350	-8.63
Diamond	$FD\bar{3}M$		1.54		109.5	3.55	431	-9.09
Graphite	$F6_3/MMC$	1.42		120		2.24	36	-9.22

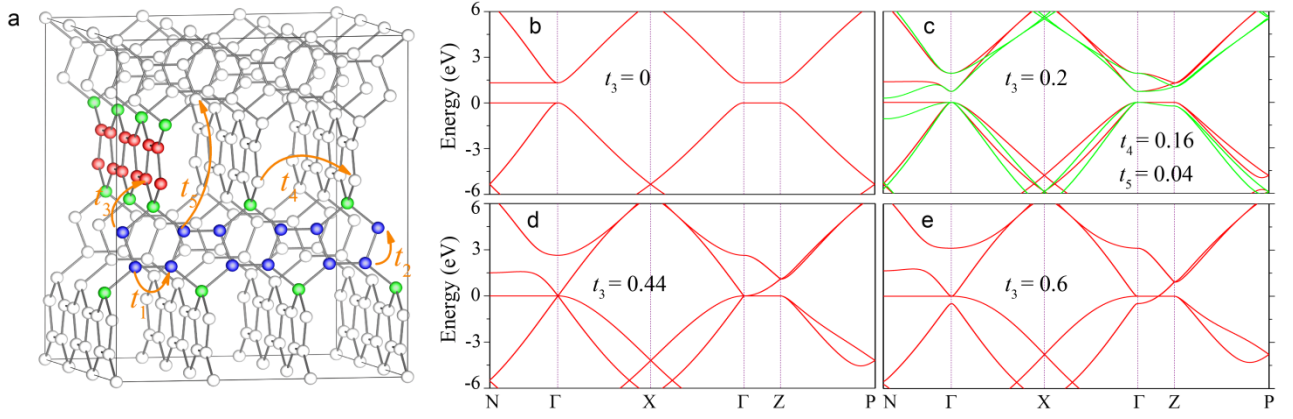
Table 1. Comparison between Pentagon Carbon and other representative Carbon allotropes. The table contains information of the space group, the bond length d (Å), the bond angle θ (°), the mass density ρ (g cm⁻³), the bulk modulus B (GPa), and the cohesive energy E_{coh} (eV per atom).



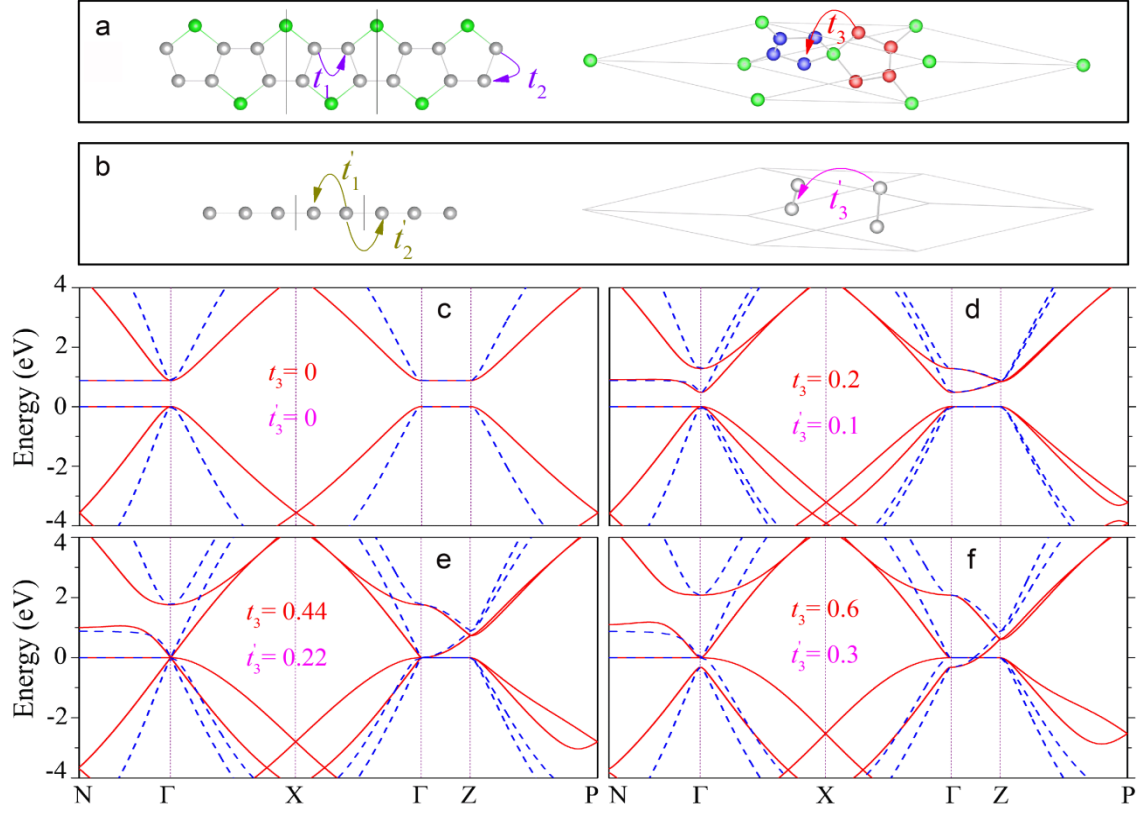
Supplementary Figure 1 | Energetic and dynamic stability of Pentagon Carbon. (a) Total energy per atom as a function of volume (equation of states, EOS) for carbon allotropes, including CKL, Bcc C8, 3D-C5, T6, Diamond, and Graphite. The EOS for each carbon structure has a local minimum, implying its state is energetic (meta-) stable. (b) Phonon dispersion of 3D-C5. There are no imaginary phonons vibrational frequencies, indicating that the structure is dynamically stable.



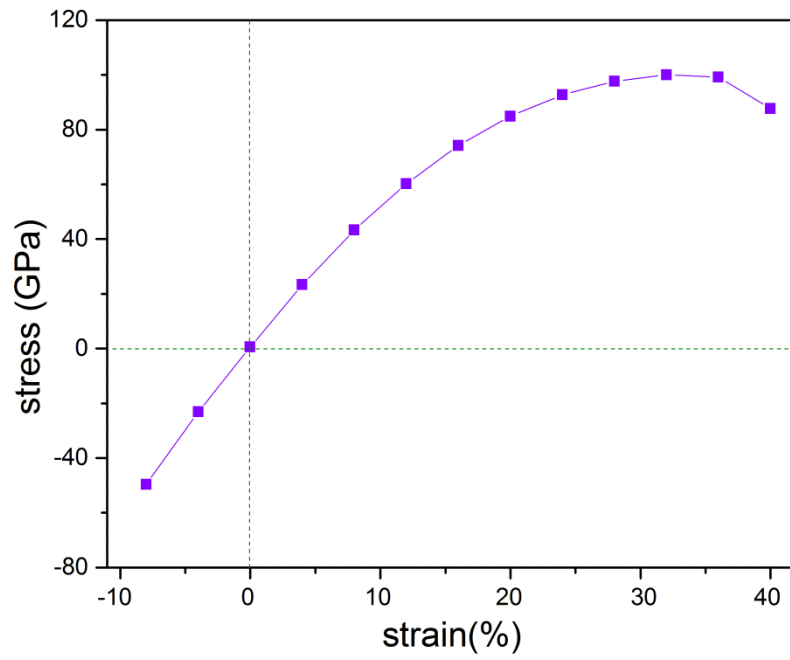
Supplementary Figure 2 | Orbital-resolved projected density of states (PDOS) near the Fermi level. The PDOS identifies the orbital contribution from each atom in the unit cell. The information is used for constructing the tight-binding model.



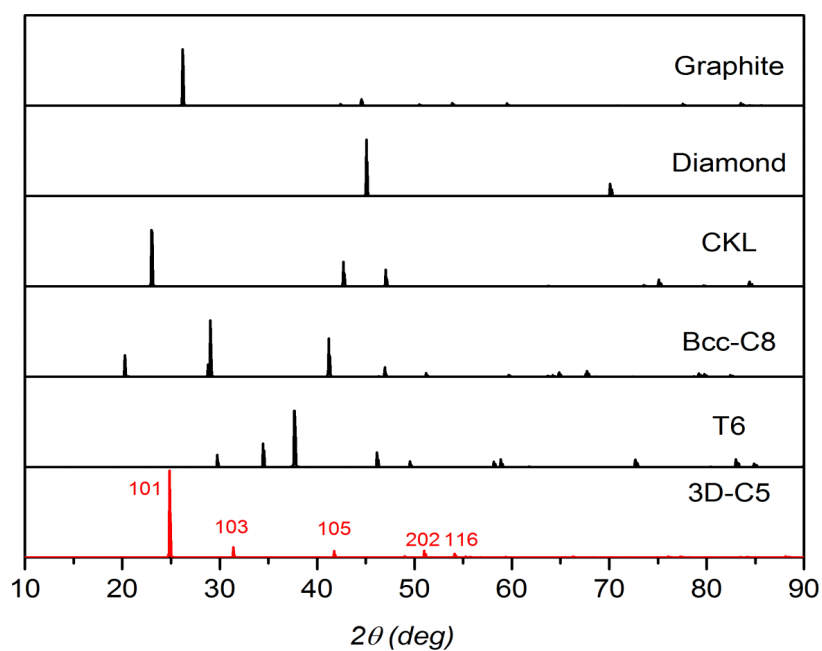
Supplementary Figure 3 | Tight-binding model and its band structures. (a) The TB model and the corresponding hopping energies. (b-e) The red lines are the results for $t_3 = 0, 0.2, 0.44$ and 0.6 eV, respectively. In all case, $t_1 = 3.04$ eV and $t_2 = -2.6$ eV. The green lines in (c) are the results of including t_4 and t_5 . According to the analytical formula, when $|t_1 + t_2| > (=, \text{ or } <) |t_3|$, the energy difference Δ (defined in the main text) is positive (zero, or negative).



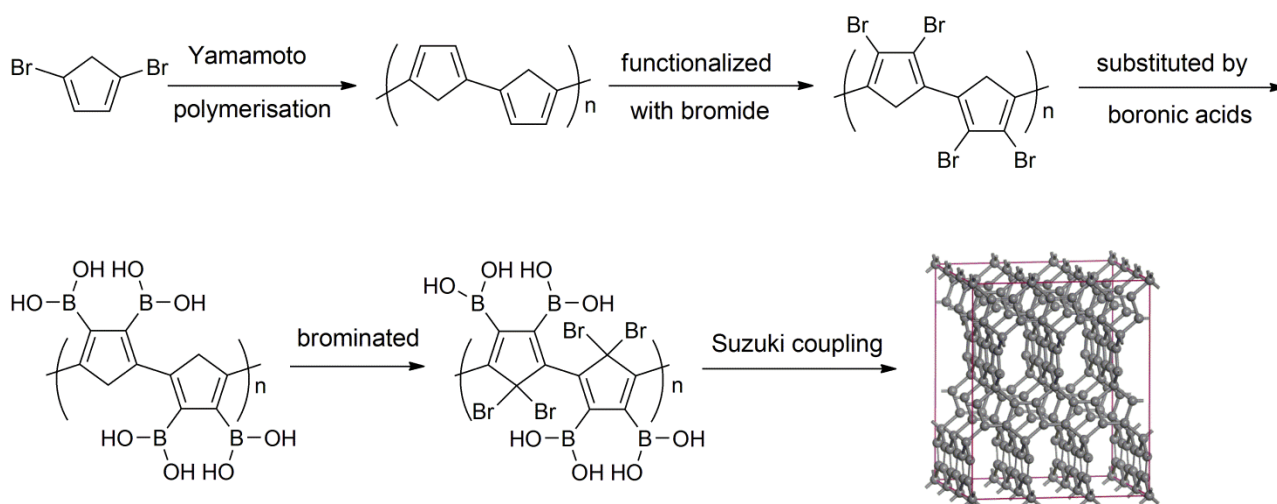
Supplementary Figure 4 | Comparison between 8-site TB model and 4-site TB model. (a) The original 8-site TB model and (b) the simplified 4-site TB model. (c-f) The band structures of the two TB models with different t_3 (t_3') values. The red solid lines and the blue dashed lines stand for the results of the original and the simplified TB models, respectively. In all case, t_1 (t_1') and t_2 (t_2') are set to 3.04 eV and -2.6 eV, respectively.



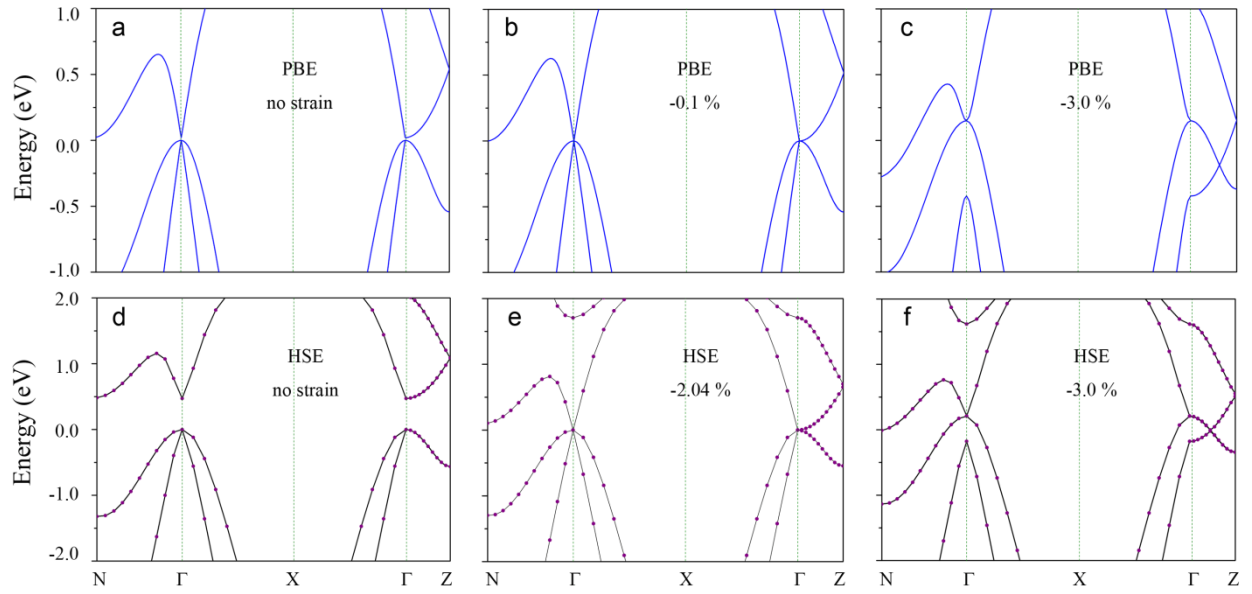
Supplementary Figure 5 | Strain-stress curve. Strain-stress relation curve of Pentagon Carbon for uniaxial strain along z -axis, showing a linear elastic regime up to 10% strain.



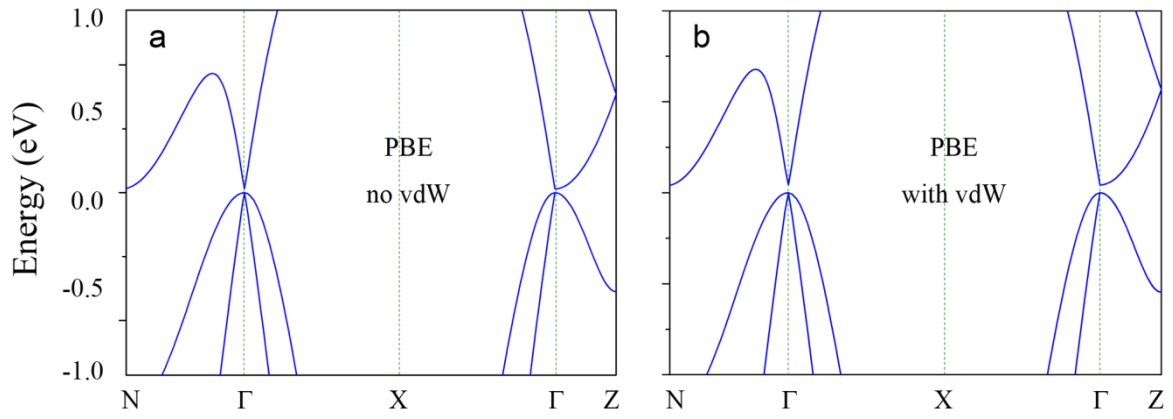
Supplementary Figure 6 | Simulated XRD patterns for representative carbon allotropes. To guide the experimental identification of Pentagon Carbon, we simulated its X-ray diffraction (XRD) pattern along with graphite, diamond, CKL, Bcc C8, T6, and 3D-C5. The simulated XRD of Pentagon Carbon (3D-C5) has a very strong peak around 24.86° correspond to the (101) diffraction. The other peaks (103), (105), (202), and (116) correspond to $2\theta = 31.48, 41.75, 51.01$, and 54.11 , respectively.



Supplementary Figure 7 | A possible reaction route for the chemical synthesis of Pentagon Carbon. First, a 1D ribbon composed of cyclopentadiene building units is synthesized by the Yamamoto polymerisation^{10, 11} of a 1,4-dibromocyclopentadiene. The 1D ribbon is functionalized with bromide by Friedel–Crafts reaction¹², which is then substituted by boronic acids. The resulting product is further brominated and connected into the predicted 3D framework through Suzuki coupling^{13, 14}. Each step in this process is either already achieved or have a high chance because of the existence of similar reactions.



Supplementary Figure 8 | Band structures calculated with PBE and HSE under different strains. (a-c) Band structure of Pentagon Carbon under uniaxial strain of (a) 0%, (b) -0.1 %, and (c) -3% at PBE level. (d-f) Result using the hybrid functional (HSE06) with uniaxial strain of (d) 0%, (e) -2.04 %, and (f) -3%. The quantum phase transition is observed at the critical strain of -2.04 % on the HSE06 level.



Supplementary Figure 9 | Comparison between calculations with and without van der Waals correction. The band structure of Pentagon Carbon (a) without and (b) with van der Waals forces. The effect of van der Waals (vdW) interaction is included in the DFT calculation with the method proposed by Grimme⁹. Since Pentagon Carbon is a 3D structure with covalently bonding, vdW interaction expected to have minor effects in the calculation results. For example, by the inclusion of vdW interaction, the cohesive energy is decreased from -8.79 eV to -8.89 eV (or by 1.1%) and the lattice parameters are decreased by about 0.2%. The main features of the band structure of Pentagon Carbon are not changed, only the bandgap is increased to about 40.5 meV with the inclusion of vdW interaction.

Supplementary Note 1: Lattice structure and stability

There are two irreducible atomic Wyckoff positions: one is the $16h$ (-0.3156, -1.0, -0.0738) site occupied by the sp^2 hybridized carbon atoms; and the other is the $4a$ (0.0, -1.0, 0.0) site occupied by the sp^3 hybridized carbon atoms. The comparison of cohesive energies as a function of volume for several representative carbon allotropes is shown in Supplementary Fig. 1a. One observes that the cohesive energy of Pentagon Carbon (3D-C5), although slightly higher than the most stable graphite and diamond, is less than $T6^1$ and $Bcc-C8^{2,3}$ and is comparable with the $CKL^{4,5}$ structure. For its mechanical property, we have calculated the elastic constant tensor in the linear elastic regime. For a tetragonal lattice system, only elastic constants C_{11} , C_{12} , C_{13} , C_{33} , C_{44} and C_{66} are independent, which are obtained as (unit GPa): $C_{11} = 459.66$, $C_{12} = 112.8$, $C_{13} = 128.3$, $C_{33} = 672.39$, $C_{44} = 113.15$, $C_{66} = 9.42$. We confirm that all these independent elastic constants satisfy the Born stability criteria^{6,7}. To further examine the dynamical stability of Pentagon Carbon, we perform calculations of its phonon spectrum. As shown in Supplementary Fig. 1b, there is no soft mode in the phonon spectrum, indicating that the proposed Pentagon Carbon structure is also dynamically stable.

Supplementary Note 2: Tight-binding model analysis

To capture the origin of the low-energy states, in Supplementary Fig. 2, we plot the projected density of states (PDOS) corresponding to the orbitals on the C1 and C2 atoms (c.f. Fig. 1c). One can find that the states around the Fermi level are mainly distributed on the C1 atoms, especially on their p_y/p_z orbitals (i.e. π orbitals), and the contribution from C2 atoms is almost negligible.

Based on the orbital analysis, we may construct a tight-binding (TB) model based on a single orbital per C1 site to capture the band features,

$$H = \sum_{\langle i,j \rangle} \sum_{\mu} t_{ij} e^{-i\mathbf{k} \cdot \mathbf{d}_{ij}^{\mu}} \quad \text{Supplementary Equation 1}$$

where $i, j \in \{1, 2, 3, \dots, 8\}$ label the eight C1 sites in a unit cell, \mathbf{d}_{ij}^{μ} is the displacement vector directed from site j to site i , t_{ij} is the hopping energy between sites i and j , and μ runs over all equivalent lattice sites under translation. We include three hopping processes: two are the nearest-neighbor hoppings along the armchair chains (t_1 and t_2); the third is between the two nearest sites of neighboring armchair chains (t_3), as indicated in Supplementary Fig. 3a. This simple model can indeed well capture the main features of the DFT result. It needs to be pointed out that the inter-chain coupling t_3 plays an important role and cannot be neglected: without t_3 , the band structure is that of uncoupled interpenetrated armchair chains and is known to be a semiconductor with a sizable gap (see Supplementary Fig. 3b); finite t_3 is required for decreasing the gap and to reproduce the observed band-splitting in the DFT result (e.g. along Γ -X, see Supplementary Fig. 3c-3e). In order to fit the DFT band structure better, one can include two more higher-order hopping processes, t_4 and t_5 , as indicated in Supplementary Fig. 3a. As one can see from Supplementary Fig. 3c, the inclusion of t_4 and t_5 makes the fitting of band dispersion along N- Γ and Γ -Z more accurate. The hopping parameters of Fig. 2a in the main text are $t_1 = 2.78$ eV, $t_2 = -2.43$ eV, $t_3 = -0.34$ eV, $t_4 = 0.15$ eV and $t_5 = 0.07$ eV, respectively. The values of t_4 and t_5 are reasonable for carbon-based materials. In

[PRB.78.205425 (2008)]⁸, the authors gave the third-nearest-neighbor tight-binding parameters for graphite and few-layer graphene. The distances of γ_1 and γ_2 are 3.35 Å and 6.7 Å, and correspondingly, the values of tight-binding parameter for γ_1 and γ_2 are 0.35 eV and -0.0105 eV, respectively. In our TB model, the distances of t_4 and t_5 are 3.715 Å and 5.601 Å, and their magnitudes of hopping energy are 0.16 eV and 0.04 eV, respectively.

We also mention that the tight-binding model may be further simplified by modeling each four-site armchair chain with a dimer chain, and the obtained simplified model can also give a reasonably good result compared with the DFT band structure. As we have mentioned in the main text, the 3D Pentagon Carbon can be viewed as consisted of orthogonal pentagon-rings ribbons, the unit cell of pentagon-ring ribbon has four C1 atoms and two different nearest-neighbor hopping energies along the armchair chain, t_1 and t_2 as depicted in the left subfigure of Supplementary Fig. 4a. In effect, we can simplify this armchair chain into a dimer atom chain with two effective hopping energies t'_1 and t'_2 as shown in the left subfigure of Supplementary Fig. 4b. As for 3D Pentagon Carbon, the eight atoms TB model can be simplified to an effective TB model with four sites, at the same time, the t_3 transform to an effective hopping energy t'_3 as denoted in right subfigure of Supplementary Fig. 4b. Eventually, the eight-site TB model can be simplified to a four-site TB model. As can be seen from Supplementary Fig. 4c-4f, these two TB models produce similar results, and both can catch the main features of the DFT band structure.

Supplementary Note 3: Results of hybrid functional method

The band structure results are verified by using the hybrid functional (HSE06) method. The comparison between PBE and HSE06 results are shown in Supplementary Fig. 6. One observes that the key features of the band structure and the phase transition are unchanged, as these are in fact dictated by the symmetry of the system. The main difference is in the quantitative band dispersion, the bandgap value, and the value of critical strain. As shown in Supplementary Fig. 6, for the unstrained system, the HSE06 bandgap is about PBE bandgap is 471.3 meV, larger than the PBE bandgap (~21.4 meV). The critical strain is also changed to about -2.04 % from the value of -0.1 % on the PBE level.

Supplementary References:

1. Zhang S., Wang Q., Chen X., Jena P. Stable three-dimensional metallic carbon with interlocking hexagons. *Proc. Natl. Acad. Sci.* **110**, 18809-18813 (2013).
2. Johnston R. L., Hoffmann R. Superdense carbon, C₈: supercubane or analog of γ -silicon? *J. Am. Chem. Soc.* **111**, 810-819 (1989).
3. Liu P., Cui H., Yang G. W. Synthesis of Body-Centered Cubic Carbon Nanocrystals. *Cryst. Growth Des.* **8**, 581-586 (2008).
4. Chen Y., *et al.* Carbon kagome lattice and orbital-frustration-induced metal-insulator transition for optoelectronics. *Phys. Rev. Lett.* **113**, 085501 (2014).
5. Zhong C., Xie Y., Chen Y., Zhang S. Coexistence of flat bands and Dirac bands in a carbon-Kagome-lattice family. *Carbon* **99**, 65-70 (2016).
6. Nye J. F. *Physical properties of crystals*. Clarendon Press (1985).
7. Wu Z.-j., Zhao E.-j., Xiang H.-p., Hao X.-f., Liu X.-j., Meng J. Crystal structures and elastic properties of superhard IrN₂ and IrN₃ from first principles. *Phys. Rev. B* **76**, 054115 (2007).
8. Grüneis A., *et al.* Tight-binding description of the quasiparticle dispersion of graphite and few-layer graphene. *Phys. Rev. B* **78**, 205425 (2008).
9. Grimme S. Semiempirical GGA - type density functional constructed with a long - range dispersion correction. *J. Comput. Chem.* **27**, 1787-1799 (2006).
10. Tsujii Y., Ohno K., Yamamoto S., Goto A., Fukuda T. Structure and Properties of High-Density Polymer Brushes Prepared by Surface-Initiated Living Radical Polymerization. In: *Surface-Initiated Polymerization I* (ed[^](eds Jordan R). Springer Berlin Heidelberg (2006).
11. Yamamoto Y., Irie M., Hayashi K. Photoinduzierte Polymerisation. 6. Mitt.

Molekulargewichtsverteilung bei der kationischen Polymerisation von α -Methylstyrol.

Colloid Polym. Sci. **256**, 396-396 (1978).

12. Olah G. A., Reddy V. P., Prakash G. Friedel - Crafts Reactions. *Kirk-Othmer Encyclopedia of Chemical Technology*, (1980).

13. Old D. W., Wolfe J. P., Buchwald S. L. A Highly Active Catalyst for Palladium-Catalyzed Cross-Coupling Reactions: Room-Temperature Suzuki Couplings and Amination of Unactivated Aryl Chlorides. *J. Am. Chem. Soc.* **120**, 9722-9723 (1998).

14. Kim S.-W., Kim M., Lee W. Y., Hyeon T. Fabrication of Hollow Palladium Spheres and Their Successful Application to the Recyclable Heterogeneous Catalyst for Suzuki Coupling Reactions. *J. Am. Chem. Soc.* **124**, 7642-7643 (2002).